Grain Boundary Sliding and Strain Rate Sensitivity of Coarse and Fine/Ultrafine Grained 5083 Aluminum Alloys

A. Goyal, V. Doquet, Amade Pouya

Grain Boundary Sliding and Strain Rate Sensitivity of Coarse and Fine/Ultrafine Grained 5083 Aluminum Alloys

A. GOYAL, V. DOQUET, and A. POUYA

The viscoplastic behavior of coarse and bimodal fine/ultrafine grained (F/UFG) Al5083 alloy was investigated between 20 °C and 200 °C through tensile tests at various strain rates, and stress relaxation tests to deduce the strain rate sensitivity (SRS). The plastic strain fields were measured by correlation of SEM images. In the F/UFG material at high temperature, very high strains were measured in shear bands which sometimes crossed the whole gage width and exhibited intensive grain boundary sliding (GBS). Both the SRS and ductility rose with the temperature, and as the strain rate decreased, mainly due to a rising contribution of GBS, which accommodated a much larger fraction of the global strain in the F/UFG material. The boundary between the temperature–strain rate domains where grain refinement led either to strengthening or to softening was determined. Finite element simulations of tension and relaxation tests with viscoplastic grains and sliding grain boundaries captured the macro-scale behavior of the F/UFG material. It also provided some insight into the mechanisms of correlated and cooperative GBS and grain rotation along percolation paths (both inter and intragranular), probably, responsible for macro shear banding.

https://doi.org/10.1007/s11661-019-05583-5

I. INTRODUCTION

ULTRAFINE grained (UFG) metals or alloys generally exhibit a substantially higher flow stress than their coarse grained (CG) counterparts, at room temperature. Their fracture strain is most often lower than that of CG materials at room temperature. However, it tends to increase as the strain rate decreases due to of a modification in the plastic strain distribution leading to a lot of diffuse—and thus harmless—micro-bands, instead of a few sharp and intense shear bands observed at higher rates.[1–3]

Regarding the high-temperature behavior of these materials, most investigations focused on the superplastic regime, characterized by a strain rate sensitivity (SRS) close to 0.5, which is controlled by grain boundary sliding (GBS)[4,5] and is observed at comparatively lower temperatures than in CG materials.[6–9] The intermediate range between room temperature and superplastic regime has, comparatively, received much less attention.

However, it has been shown by Kapoor *et al.*[10] that above a strain rate-dependent temperature, instead of GBS-induced hardening, GBS-induced softening occurs in Al-1.5Mg,. Since many potential applications of UFG alloys involve heating above ambient temperature, it is necessary to determine the temperature and strain rate domains in which a beneficial effect of the ultrafine microstructure can be expected. This is one of the purposes of this study on Al 5083 alloy.

Since the evolutions in ductility with strain rate mentioned above seem to correlate with the degree of strain localization, and thus to the SRS, this parameter was measured as a function of temperature and strain rate, through stress relaxation tests in CG and UFG Al 5083 alloys. The plastic strain fields in these materials were measured by digital image correlation (DIC) before and after tensile tests run at room or high temperature. The discontinuities induced by GBS along the micro-grids laid on the surface for digital image correlation (DIC) were used to estimate the contribution of GBS to the overall deformation, which appeared to explain most of the temperature and strain rate-dependence of the SRS.

In the seventies, Raj and Ashby[11] proposed an analytical model of grain boundary sliding accommodated either elastically, or by diffusion. They formulated a linear, threshold-free relation between the GB sliding

A. GOYAL and V. DOQUET are with the Laboratoire de Mécanique des Solides, UMR 7659 CNRS, Ecole Polytechnique, 91128, Palaiseau, France. Contact e-mail: doquet@lms.polytechnique.fr A. POUYA is with the Laboratoire Navier (IFSTTAR, CNRS, ENPC), Paris-Est University, 77455 Champs sur Marne, France.

Manuscript submitted August 30, 2019.

Journal : MMTA Dispatch : 3-12-2019 Pages : 14
PIPS No. : 5583 ☐ LE ☐ TYPESET
MS Code : ☐ CP ☐ DISK

rate and the resolved shear stress, in which viscosity increased with the roughness of the GB, and with the presence of second phase particles along its length. Ashby and Verrall[12] introduced a GBS-induced neighboring grains switching mechanism, without any elongation or change in crystal orientation. They predicted a grain size-dependent evolution of the SRS associated with the transition from this deformation mechanism to dislocation-controlled creep, as the strain rate rises.

A 2D, plane strain finite element analysis of creep with free grain boundary sliding accommodated by elasticity and diffusion processes was later developed by Crossman and Ashby,[13] who considered a regular array of hexagonal grains with power law creep inside. They investigated the influence of the viscous stress exponent, n, inside the grains, and of the strain rate on the contribution of GB sliding to the overall deformation. They obtained a modified power law equation for the steady creep rate that predicts an acceleration when GBS occurs, but no modification of the creep exponent. The 2D computational approach of Tvergaard[14,15] in the eighties was close to that of Crossman and Ashby, but laid emphasis on the consequences of GB sliding in terms of cavities nucleation and growth along the grain boundaries normal to the tensile axis, while Hsia *et al.*[16] directly introduced a density, of micro-cracks along such GBs and investigated the effect of GB sliding on the growth rate of such cracks. All the works mentioned above considered a periodic array of hexagonal grains.

Onck and Van Der Giessen[17] investigated the effect of microstructural variations on the creep rate of a polycrystalline aggregate with freely sliding boundaries, by slightly perturbing an initially regular array of hexagonal grains. The computed creep rate was enhanced by up to 60 pct by the introduction of some irregularity, due to increased GB sliding.

Bower and Wininger[18] proposed a sophisticated 2D crystal plasticity finite element (CPFE) approach where, in addition to GB sliding, GB migration assisted by diffusion was modeled. They used a front tracking scheme and adaptive mesh generation techniques to follow the changes in grain structure. The model was used by Agarwal *et al.*[19] to predict the rate-sensitive SRS of fine-grained (7 to 10 μm) Al5083 alloy above 450 °C. Some discrepancies with experimental data were found at low strain rate, but according to Du *et al.*[20] the introduction of a threshold shear stress for GB sliding improved the predictions. Both studies were based on the same polycrystalline aggregate with 18 irregular grains, taken from a micrograph, as well as the crystal orientations. The simulations were not repeated with different numbers of grains and different sets of orientations, so that their statistical representativeness can be questioned. In addition, only {111} (110) slip was considered, while non-octahedral slip systems were found to operate above 200 °C in Al 5083 alloy.[21]

Many authors used molecular dynamics (MD) simulations to investigate GB mobility. Qi and Krajewski[22] used MD to simulate GBS in aluminum at 750 K and reported three regimes depending on the applied stress: (i) at low applied stress, no sliding was observed, indicating the existence of a threshold stress (ii) at intermediate stress, the amount of sliding increased linearly with time, confirming the linear viscous nature of GBS described by Raj and Ashby, and (iii) at high stress, the amount of sliding increased parabolically with time. According to the MD simulations done by Du *et al.*[23] the segregation of solute atoms (Mg and Si in Al5083 alloy) at GBs affects the threshold stress for GB sliding. While these atomic scale simulations provide valuable insight into the GB deformation mechanisms and their variations from one type of GB to another, it is difficult to get quantitative data, since the simulations are run at pico-seconds time scales and generally include only two neighboring grains, without any triple point, as in a polycrystal.

A solution for scale transition was proposed by Warner *et al.*[24] who performed 2D "atomistics-informed" crystal plasticity finite element (CPFE) simulations for nano-crystalline copper, with 200 grains and GB constitutive equations derived from prior MD simulations. However, since MD simulations were run for a few specific types of GB (symmetric or asymmetric tilt boundaries), the shear strength of high-angle GBs in CPFE simulations was assigned randomly. A "thermal correction" to the 0 K molecular statics results had to be applied, since the stress levels computed with MD at very high strain rates and 0 K are unrealistically large.

Compared to these sophisticated micromechanical approaches, the 2D finite element model including GBS in a phenomenological way developed in the present work is quite simplified. However, it will be shown to capture the mechanical behavior of UFG Al 5083 between 20 °C and 200 °C, in a wide range of strain rates, and to provide some insight into the cooperative phenomena (GBS and grain rotation).

II. EXPERIMENTAL STUDY

A. *Experimental Procedures*

A cast and annealed plate of Al-5083 alloy (with the composition shown in Table I) was used to machine specimens of CG material, or rods for ECAP processing. This as-received material had equiaxed grains with a mean size of 93 μm, and contained coarse dendritic intermetallic particles, mostly along the grain boundaries, as shown in Figure 1.

20 × 20 mm rods cut from the plate were submitted to 3 ECAP passes at room temperature, with a back pressure of 60 MPa, following route C (rotation of the sample by 180 deg between consecutive passes), in a lubricated die, with an angle of 90 deg. The material was then annealed at 200 °C during 6 hours. The resulting microstructure was partly characterized by EBSD, in a Philips Quanta 600 FEG-ESEM, using the hkl software, a tension of 20 KV and a step size of 75 nm. A typical orientation map in a small area along the insertion axis/exit axis plane is presented in Figure 2(b). It proved difficult to reach a good indexation rate with EBSD, but Transmission Kikuchi Diffraction (TKD) on a FIB-cut thin foil allowed a more accurate characterization, and confirmed the grain size statistics issued from EBSD

Journal : MMTA Dispatch : 3-12-2019 Pages : 14
PIPS No. : 5583 ☐ LE ☐ TYPESET
MS Code : ☐ CP ☐ DISK

data collected on 100 × 100 μm areas along 3 orthogonal planes. The mean grain size was 680 nm, but the microstructure was heterogeneous, with areas in which the mean grain size was around 300 nm, as well as less refined areas, with micron-sized grains (Figure 2(c)). The fraction of high-angle grain boundaries (*i.e.*, with a misorientation larger than 15 deg) was around 65 pct. This fine/ultrafine bimodal microstructure will be denoted by F/UFG in the following. The grains were elongated in the shearing direction of ECAP, at an angle around 55 deg. The intermetallic particles were broken or debonded and formed rows along the shearing direction of ECAP (Figure 2(a)).

Table I. Chemical Composition of Al 5083 Alloy

Composition	Weight Percent
Mg	5.2
Fe	0.24
Mn	0.45
Si	0.27
Cr	0.09
Al	balance

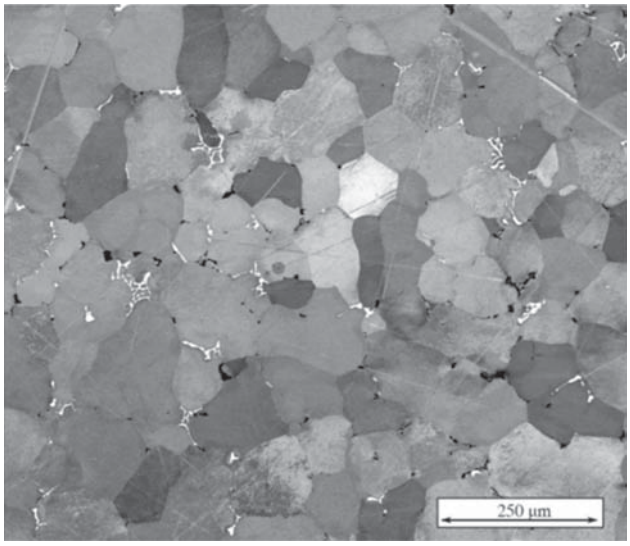

Fig. 1—Microstructure of coarse grained Al5083 Al alloy.

Flat dog-bone shaped specimens, with a 17 mm long and 4 mm wide gage length, as well as 8 mm high cylindrical specimens with a diameter of 8 mm were machined parallel to the extrusion axis for tensile tests and relaxation tests in compression, respectively. The surface of the dog-bone specimens was electro-polished. To measure the strain fields using digital image correlation (DIC), several 600 × 600 μm patches of gold grids with a 5 μm pitch were printed along the gage length, using E-beam lithography. 4096 × 3775 pixels SEM images of the 600 × 600 μm^2 areas covered with grids were captured before and after the tensile tests. The image resolution was thus around 146 nm $pixel^{-1}$. The CmV DIC software[25] was used with a subset size of 4.4 × 4.4 μm^2.

The tests at high temperature were run on a servo-hydraulic machine equipped with a thermal chamber. The tests were displacement-controlled, and the tensile tests were run at different rates, chosen, based on available data from the literature, so as capture the transition from GB-induced strengthening to GB-induced softening, at each temperature. The sample strain was measured by monitoring the relative displacement of two dots painted near the ends of the gage length. SEM images of the micro-grids captured before and after the tensile tests were used for DIC.

The relaxation tests were performed in compression on cylindrical specimens lubricated with a Teflon spray. The samples were first deformed in compression with a constant displacement rate corresponding approximately to a strain rate of 2×10^{-3} s^{-1} up to 3 to 5 pct strain. Then the crosshead displacement was stopped for 2 hours, while the stress and strain were recorded, each time the load changed by 50 N. Since the tests were displacement-controlled, the plastic strain

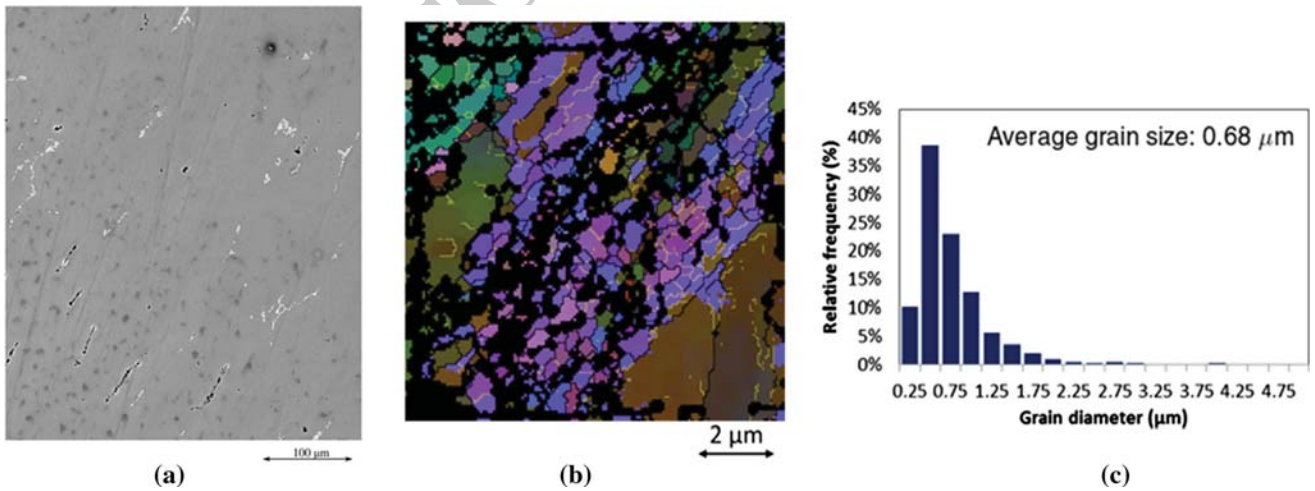

Fig. 2—Microstructure of F/UFG 5083 Al alloy, (*a*) elongated intermetallic particles, (*b*) EBSD map (Euler angles), and (*c*) grain size distribution.

Journal : MMTA Dispatch : 3-12-2019 Pages : 14
PIPS No. : 5583 ☐ LE ☐ TYPESET
MS Code : ☐ CP ☐ DISK

rate, $\dot{\varepsilon}_p$ was calculated using the method proposed by Lee and Hart[26] as:

$$\dot{\varepsilon}_p = -\frac{\dot{\sigma}}{\left[\frac{Kh}{A} - \sigma\right]}, \quad [1]$$

where σ is the true stress, K the combined stiffness of the machine and the sample, and A and h are the cross-section and height of the specimen, respectively. The strain rate sensitivity:

$$S = \frac{\partial \ln \sigma}{\partial \ln \dot{\varepsilon}} \quad [2]$$

was calculated from the slope of plastic strain rate *vs* true stress bi-logarithmic plots.

B. *Macro-scale Behavior*

Figure 3 compares the tensile curves of CG and F/UFG alloys at various strain rates, at 20 °C, 100 °C, and 200 °C. Both materials exhibited serrated flow, due to dynamic strain aging induced by solute Mg atoms. At room temperature, grain refinement significantly increased the flow stress, and reduced the ductility, as generally reported in the literature for F/UFG alloys. At 100 °C, the difference in flow stress between the two microstructures was reduced, and at 200 °C, the tensile curves of the F/UFG alloy lied above or below that of the CG alloy, depending on the strain rate. For a given temperature, ductility was strongly strain rate-dependent, as discussed below. Necking was very limited, and fracture was generally slanted.

Figure 4 shows the evolution of the plastic strain rate with the true stress during the relaxation tests run at various temperatures on CG and F/UFG materials. The curves are neither straight nor parallel, which reveals evolutions of the strain rate sensitivity with the temperature as well as with the strain rate. These evolutions are represented in Figure 5. For a given temperature and strain rate, the SRS was higher in the F/UFG material. In both materials, it rose with the temperature and, at a given temperature, with decreasing strain rate.

Using tension and relaxation data, the temperature and strain rate domains in which microstructure refinement leads to strengthening (low temperature, high strain rate regime) or to softening (high temperature, low strain rate regime) were identified and plotted on Figure 6. Data from Ko *et al.*[6] for the same alloy and from Kapoor *et al.*[27] for Al-1.5Mg are also plotted, and are in good agreement with the present results.

As mentioned above, in both materials, ductility above 100 °C increased as the strain rate decreased. The SRS also rose as the strain rate decreased, and a linear correlation was found between ductility and SRS, for each material, as shown in Figure 7. Fracture was thus controlled by strain localization, that a high SRS tends to hinder.

C. *Micro-scale Strain Distribution and Deformation Mechanisms*

Figure 8 compares strain fields measured in both materials, at room temperature after a few percent tensile strain, at 5.8×10^{-5} s^{-1}. In the CG alloy, the fracture of intermetallic particles located along the grain boundaries triggered strain localization in short bands connecting them, without any preferential orientation.

By contrast, in the F/UFG alloy, intermetallic particles, already broken or debonded by ECAP, and aligned in the same direction as the elongated grains, triggered the formation of hundreds of micron-long shear bands. At this temperature (0.34 $T_{melting}$), grain boundary sliding in this material produced measurable discontinuities in the grids only in stress concentration areas, near fractured particles (Figure 9).

At 100 °C (0.43 $T_{melting}$) and above, GB sliding was observed in the CG material (Figure 10).

To estimate the frequency of this phenomenon, the number of sliding GBs intercepted by a series of parallel lines was counted, and was divided by the total number of GBs intercepted by the same lines. To estimate the strain due to GBS, the micro-grids shifts, u, parallel to the tensile axis were measured along a series of transverse grid lines of total length t, and Bell and Langdon's formula[28]:

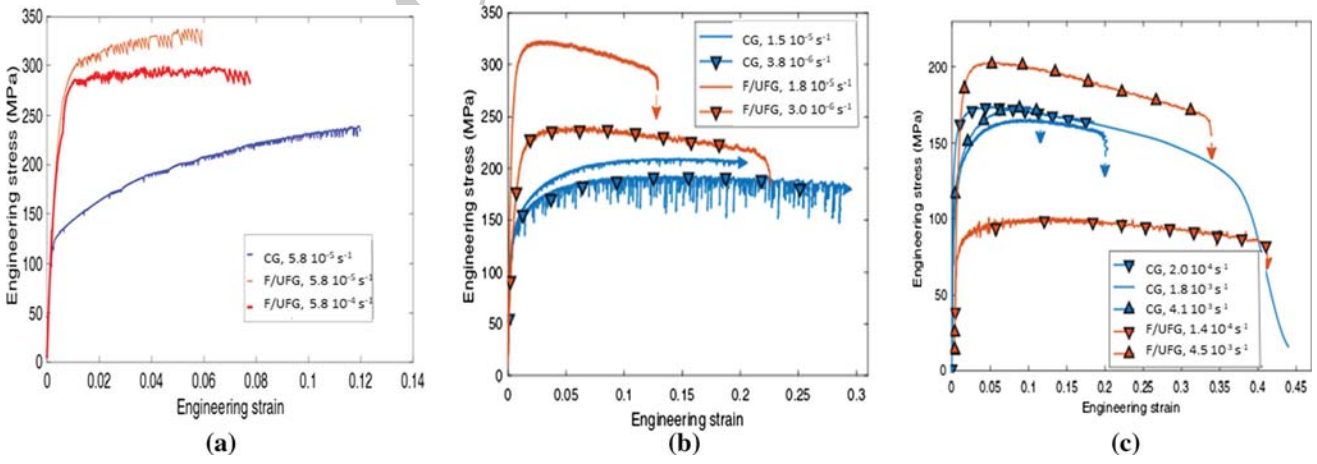

Fig. 3—Tensile curves (*a*) at room temperature, (*b*) 100 °C, and (*c*) 200 °C.

Journal : MMTA Dispatch : 3-12-2019 Pages : 14
PIPS No. : 5583 ☐ LE ☐ TYPESET
MS Code : ☐ CP ☐ DISK

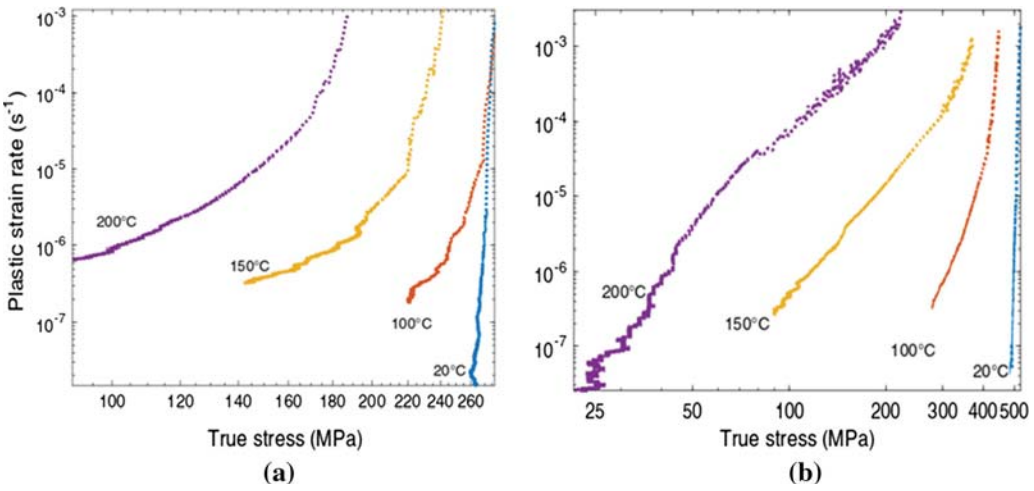

Fig. 4—Stress relaxation curves for (*a*) CG and (*b*) F/UFG materials.

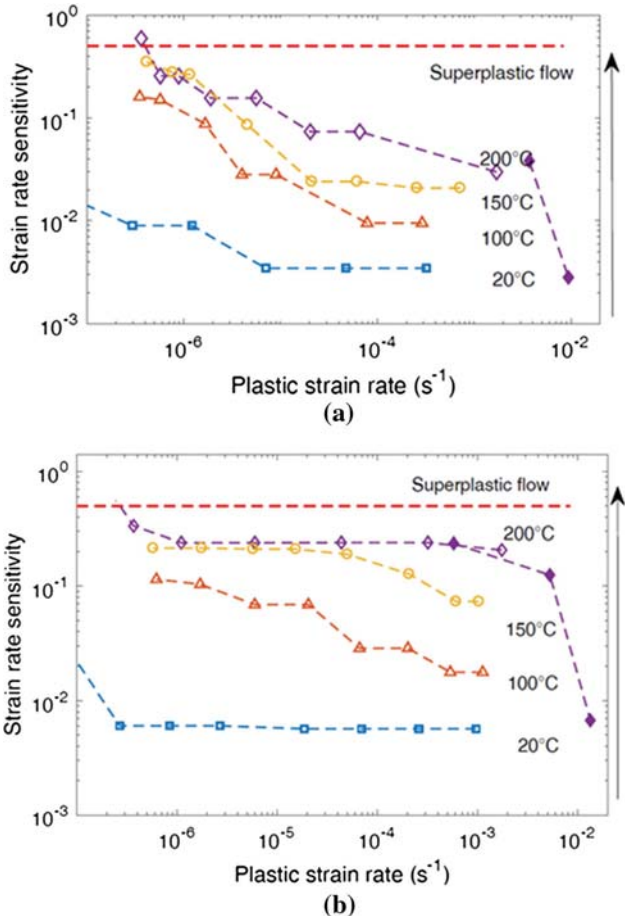

Fig. 5—Evolutions of the strain rate sensitivity for (*a*) CG and (*b*) F/UFG materials.

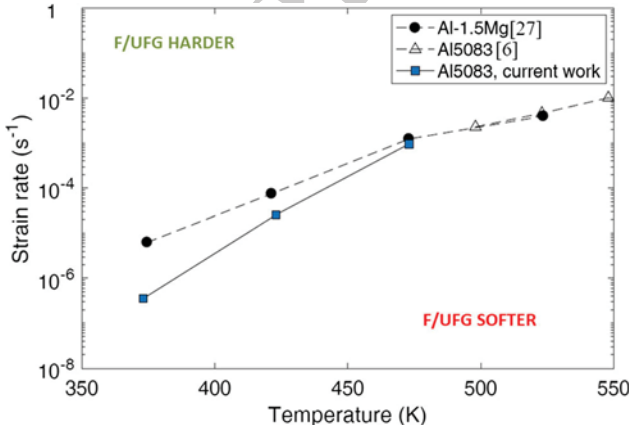

Fig. 6—Domains of grain boundary-induced hardening or softening.

$$\varepsilon_{GBS} = \frac{1}{t}\sum_{0}^{t} u \times \tan(\theta), \qquad [3]$$

where θ denotes the angle between a grain boundary and the tensile axis—was used. At 100 °C, 9.5 pct of the GBs had sled after 6 pct tensile strain at 1.5×10^{-5} s^{-1}, but this mechanism accounted only for 0.6 pct of the global strain. At 200 °C (0.55 $T_{melting}$) 44 to 68 pct of the grain boundaries had sled, depending on the strain rate and strain level, but the contribution of this mechanism to the global strain remained limited to 0.8 to 3.8 pct, as reported in Table II.

Figure 11 shows strain maps in F/UFG samples deformed to fracture at 100 °C and 200 °C. Very high strains—up to 50 pct at 100 °C and 90 pct at 200 °C—are measured inside shear bands that sometimes cross the whole gage width.

Strain localization and void sheeting inside such bands led to slanted fracture. A zoom inside such a band reveals intensive grain boundary sliding (Figure 12).

The method described above was used to estimate the contribution of GBS to the global strain. Since the orientation of each sliding GB was difficult to measure

Journal : MMTA Dispatch : 3-12-2019 Pages : 14
PIPS No. : 5583 ☐ LE ☐ TYPESET
MS Code : ☐ CP ☐ DISK

in that case, a common value of 55 deg representative of the orientation of GBs after ECAP was assumed for the angle θ in Eq. [3]. The results are reported in Table III.

While for the CG alloy, GBS accounted for less than 4 pct of the global strain, in the F/UFG alloy, it accounted for up to 29 pct (and even up to 80 pct within intense shear bands). As expected of a thermally-activated phenomenon, it increased with the temperature, and for a given temperature, as the strain rate decreased.

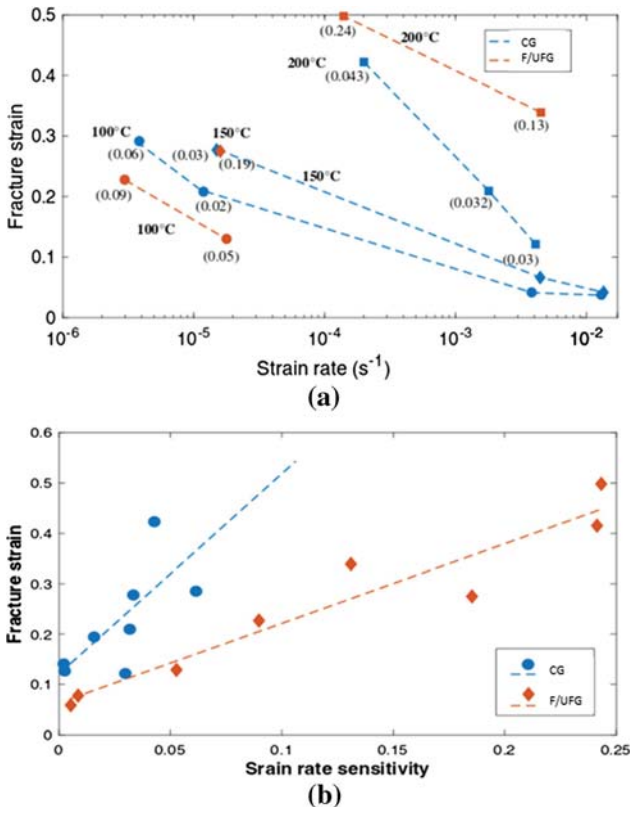

Fig. 7—(*a*) Effect of the strain rate on ductility, and (*b*) correlation of ductility with the SRS.

For the F/UFG alloy, the measured SRS correlates directly with the contribution of GBS, as illustrated by Figure 13.

III. MODELING AND SIMULATION

A 2D, infinitesimal strain, plane stress model with an isotropic viscoplastic behavior for the grains and elastic-viscous sliding interfaces was developed, using the DISROC finite element code.[29] No attempt to capture the mechanical anisotropy probably induced by the crystallographic texture inherited from ECAP was made. The aim was rather to capture the effects of strain rate and temperature on the uniaxial macroscopic response of the F/UFG material, and to use the

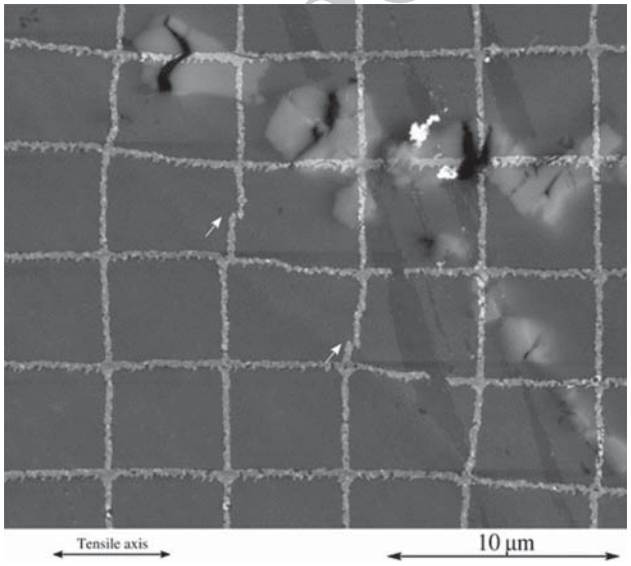

Fig. 9—Grain boundary sliding at room temperature in the F/UFG material triggered locally by the stress concentration near broken intermetallic particles.

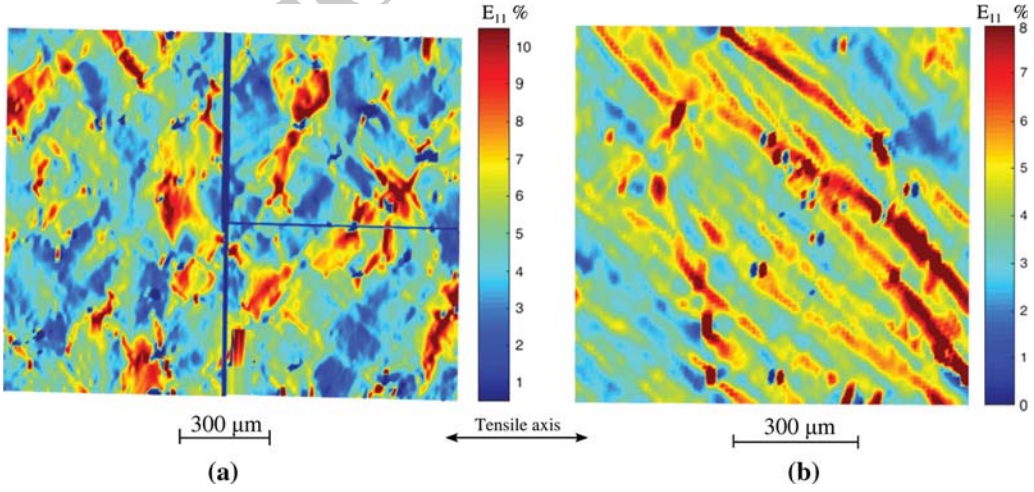

Fig. 8—Strain fields measured at room temperature during tensile tests at 6×10^{-5} s^{-1} (a) in the CG materials strained by 5.1 pct and (*b*) in the F/UFG material strained by 4.3 pct.

Journal : MMTA Dispatch : 3-12-2019 Pages : 14
PIPS No. : 5583 ☐ LE ☐ TYPESET
MS Code : ☐ CP ☐ DISK

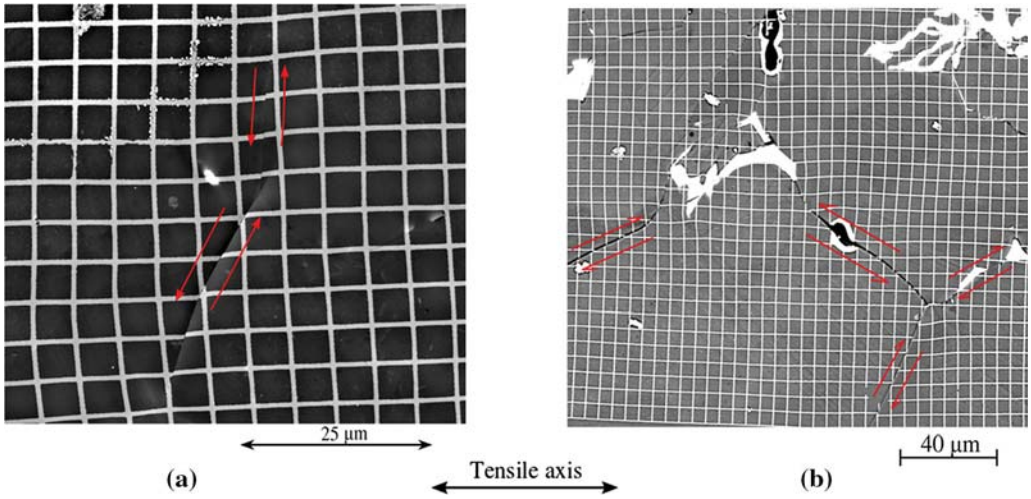

Fig. 10—Grain boundary sliding in CG samples: (*a*) after 6.5 pct strain at 1.5×10^{-5} s^{-1} at 100 °C and (*b*) after 4.7 pct strain at 7×10^{-6} s^{-1} at 200 °C.

Table II. Fraction of Sliding GBs and Contribution of GBS to the Global Plastic Strain in the CG Material, Depending on Temperature, Strain, and Strain Rate

T (°C)	Strain Rate (s^{-1})	Strain Level (Pct)	Pct of Sliding GBs (Pct)	Contribution of GBS (Pct of Global Strain) (Pct)
100	1.5×10^{-5}	6	9	0.6
200	4.1×10^{-3}	12	44	0.8
200	1.8×10^{-3}	23	68	1.8
200	7.0×10^{-6}	5	55	3.8

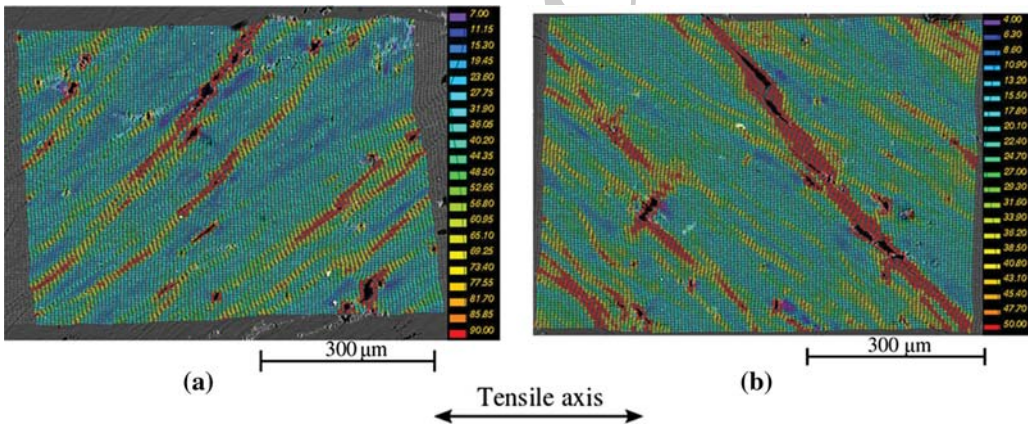

Fig. 11—Strain fields measured in F/UFG samples (*a*) at 100 °C, after 22.7 pct strain at 3×10^{-6} s^{-1} and (*b*) at 200 °C after 33.9 pct strain at 4.5×10^{-3} s^{-1}.

identified model to investigate micro-scale cooperative phenomena (in terms of GBS and grains rotation) and their effects on the heterogeneity of the strain field. Crystal plasticity was thus not used, for the reasons evoked in the introduction: lack of representativeness of a single set of orientations that would call for repeated simulations, lack of data on non-octahedral slip systems, known to be active at the temperatures of interest.

In a first stage, to calibrate the model, adjust mesh parameters and investigate the effect of the number of simulated grains, equiaxed grains with a nearly uniform size were considered. In a second stage, the model was applied to more realistic grains morphologies, inspired from the EBSD mapping shown on Figure 2.

A. *Mesh and Boundary Conditions*

For the first stage, various equiaxed microstructures were randomly generated using the classical Voronoi tessellation method. The mean grain size was controlled by the area of the simulation box, A_{box} and the number of grains, N:

Journal : MMTA Dispatch : 3-12-2019 Pages : 14
PIPS No. : 5583 ☐ LE ☐ TYPESET
MS Code : ☐ CP ☐ DISK

$$d_{\text{grain}} = \sqrt{\frac{A_{\text{box}}}{N}} \quad [4]$$

It was adjusted to 680 nm, the mean grain size measured for the F/UFG material. A mesh with linear triangular elements for the grains and linear quadrilateral elements for the grain boundaries was adopted. After a convergence study, an element size equal to 0.01 times the simulation box edge was chosen along the GBs, and 0.05 times the simulation box edge for grains cores (Figure 14(a)).

Figure 14(a) presents the boundary conditions and loadings. The bottom left corner node was fixed and the vertical displacement of the bottom line was zero. A constant vertical displacement rate, $\dot{U}_y$, corresponding to a constant global strain rate, $\dot{\varepsilon}$ was imposed at the top line, to simulate tensile tests, while a constant vertical displacement, corresponding to a fixed strain was applied to simulate stress relaxation. Due to the unavailability of periodic boundary conditions in the Disroc FE code, the left and right borders were free surfaces. One of the shortcomings of these boundary conditions was that the motions of GBs cutting a side surface are unconstrained and thus more pronounced than for GBs ending inside the model, while, conversely, sliding of those cutting the upper or lower surface is more constrained. This bias however got smaller and smaller as the number of grains increased.

In a second stage, a more realistic microstructure with 262 grains (Figure 14(c)), inspired from the EBSD map shown on Figure 2(b), was designed, using the Voronoï tessellation method, but with the measured center of gravity of the grains used as "seeds" in the algorithm, instead of points randomly generated by a Poisson's process. This makes it possible to take into account the heterogeneity of grains size and their elongated morphology. In addition, to reduce the above-mentioned artifact associated with unconstrained/over-constrained sliding of GBs cutting the sides of the model, a uniform buffer layer of material without sliding GBs, but with the same behavior as the grain cores was added all around, and the boundary conditions were applied on its external contour. The thickness of this external layer was equal to 1 grain diameter *i.e.*, for 262 grain model it was 6.2 pct of the edge of the central part.

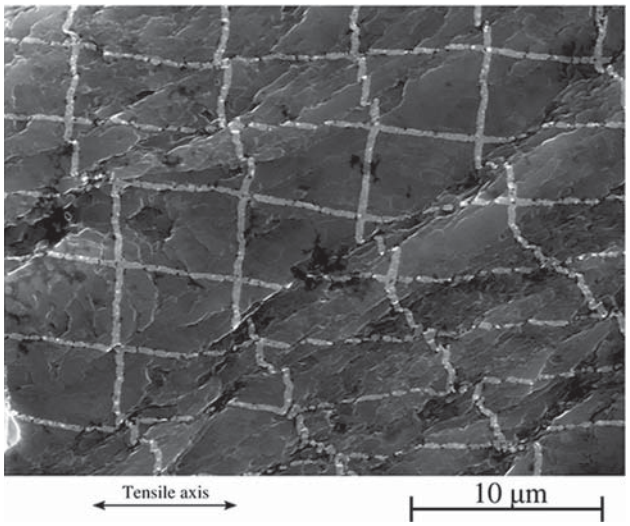

Fig. 12—Grain boundary sliding inside a shear band in a F/UFG sample strained by 49.8 pct at 200 °C at 1.4×10^{-4} s^{-1}.

B. *Constitutive Equations for the Grains*

The strain rate inside a grain was decomposed into elastic, plastic, and viscous components:

$$\dot{\varepsilon}_g = \dot{\varepsilon}_{el,g} + \dot{\varepsilon}_{p,g} + \dot{\varepsilon}_{v,g}. \quad [5]$$

The Young's modulus $E(T)$ was temperature-dependent, while the Poisson's ratio, ν, was assumed to remain constant. An isotropic strain hardening model was chosen. A Voce-type hardening function was adopted for the isotropic hardening variable, R:

$$R = R_0 + Q(1 - e^{-bp}), \quad [6]$$

where R_0, Q and b are material constants, and p denotes the cumulated plastic strain. Von-Mises yield criterion is chosen. The yield function was thus:

$$\sqrt{3J_2(\sigma)} - R = 0. \quad [7]$$

The viscous strain inside the grains was calculated using an Arrhenius-type equation with power law in effective stress:

$$\dot{\varepsilon}_{v,g} = a(\sigma - \sigma_c)^n, \quad [8]$$

where a and σ_c are temperature-dependent material parameters.

Table III. Contribution of GBS to the Global Plastic Strain in the F/UFG Material, Depending on Temperature, Strain, and Strain Rate

T (°C)	Strain Rate (s^{-1})	Strain Level (Pct)	Contribution of GBS (Pct of Global Strain) (Pct)
100	1.8×10^{-5}	12.9	9
100	3.0×10^{-6}	22.7	13
150	1.6×10^{-5}	27.5	22
200	4.5×10^{-3}	33.9	18
200	1.4×10^{-4}	49.8	29

Journal : MMTA Dispatch : 3-12-2019 Pages : 14
PIPS No. : 5583 ☐ LE ☐ TYPESET
MS Code : ☐ CP ☐ DISK

1. *Constitutive equations for the grain boundaries*

The displacement rate vector at a grain boundary had an elastic and a viscous component:

$$\dot{U} = \dot{U}_{el} + \dot{U}_{v}. \quad [9]$$

The tangential and normal stresses were related to the elastic displacement by an elastic stiffness matrix, K:

$$\begin{pmatrix} \tau \\ \sigma \end{pmatrix} = \begin{pmatrix} K_t & K_{tn} \\ K_{nt} & K_n \end{pmatrix} \begin{pmatrix} U_t - U_{t,v} \\ U_n - U_{n,v} \end{pmatrix} \quad [10]$$

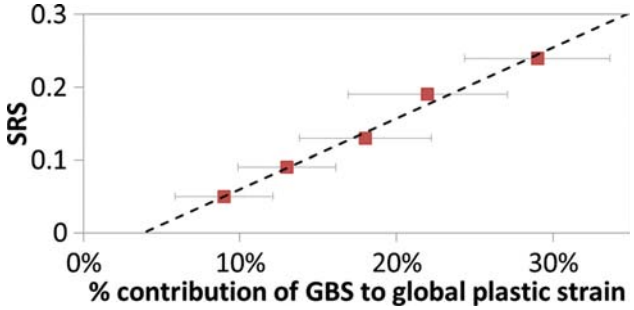

Fig. 13—Correlation between the strain rate sensitivity of the F/UFG alloy and the measured contribution of grain boundary sliding to its global deformation.

No tension-shear coupling was introduced, *i.e.*, both K_{nt} and K_{tn} were taken equal to zero. To limit the interpenetration of neighboring grains in case of normal compression, a hyperbolic expression was adopted for the normal stiffness, K_n.

$$K_n = \frac{K_0}{1 + \frac{U_n}{e}}, \quad [11]$$

where K_0 and e are constants. The closure displacement was thus limited by the initial (purely computational) "thickness", e of the interface, taken as 1 pct of the simulation box size. Closure corresponds to negative values of U_n. The normal stiffness, K_n approaches infinity when the closure displacement, U_n tends to $-e$. The normal stress is proportional to the normal displacement for small openings (with a proportionality constant K_0) and saturates at $K_0 e$ for large positive openings (never reached in the present simulations). In order not to modify the global elastic behavior by elastic GBS, the GB elastic stiffness parameters, K_0 and K_t were not independent, but related to the Young's and shear modulus, respectively.

For the viscous part, no normal creep was allowed, only viscous sliding was considered. A temperature-dependent threshold was introduced, *i.e.*, the sliding rate

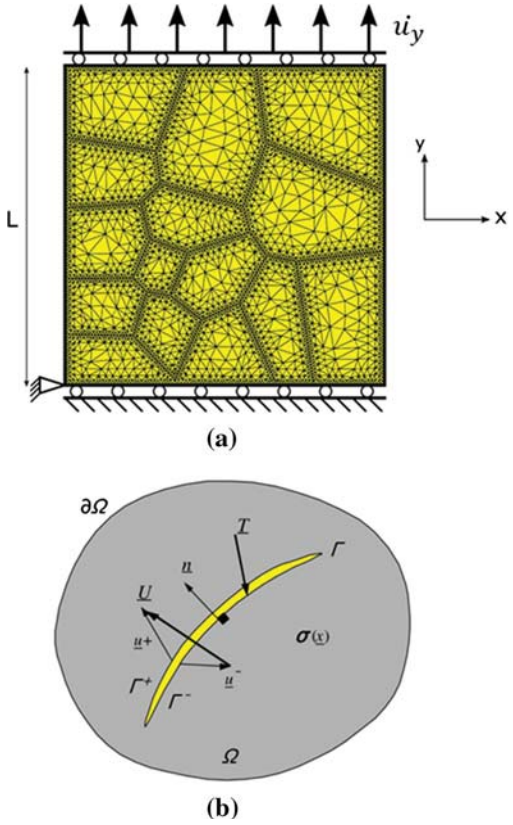

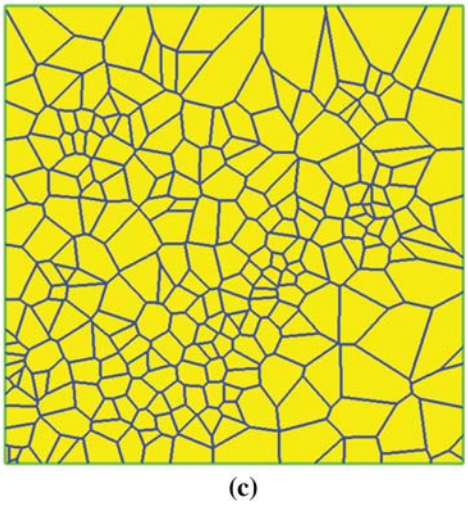

Fig. 14—(*a*) Example of mesh and boundary conditions used for the model calibration stage, (*b*) description of a sliding interface, and (*c*) more realistic microstructure inspired from the EBSD mapping shown on Fig. 2(b).

Journal : MMTA Dispatch : 3-12-2019 Pages : 14
PIPS No. : 5583 ☐ LE ☐ TYPESET
MS Code : ☐ CP ☐ DISK

was supposed to be zero if the shear stress did not reach the threshold stress, τ_c, and was proportional to the net shear stress otherwise.

$$\dot{U}_{t,v} = b_t \langle \tau - \tau_c \rangle. \quad [12]$$

To take into account the thermally-activated nature of GB sliding, an Arrhenius-type expression inspired from the work of Raj and Ashby[11] and Agarwal *et al.*[19] was assumed for the proportionality constant:

$$b_t = \frac{b_0}{kT} e^{\frac{-Q_{GBS}}{kT}}, \quad [13]$$

where b_0 is a material parameter (6.64×10^{-28} m^4 s^{-1}, according to Reference 18), Q_{GBs} is the activation energy for GBS (1.4×10^{-19} J, according to Reference 18) and k is Boltzmann's constant.

The macroscopic viscoplastic strain E_{vp} sees the contributions from the matrix viscoplastic strain and from the viscous displacement jumps U_k across sliding interfaces of contour Γ_k and normal n_k (Figure 14(b)):

$$E_{vp} = \frac{1}{V}\left[\int_V \varepsilon_{vp} \cdot dV + \sum_k \int_{\Gamma_k} \frac{1}{2}(U_{v,k} \otimes n_k + n_k \otimes U_{v,k}) ds\right]. \quad [14]$$

The contribution of GBS to the global viscoplastic strain can thus be computed as the second term of the right hand side of Eq. [14] divided by E_{vp}.

2. *Determination of the minimum number of simulated grains for convergence*

To determine the minimum number of grains required in the model so as to get rid of the scatter from one randomly-generated microstructure to the other—in terms of global stress–strain behavior, but also in terms of predicted contribution of GBS—, five different microstructures each with 15, 22 and 30 grains of similar mean grain size were randomly generated (Figure 15(a)). A tensile test up to 10 pct strain was simulated at 5×10^{-3} s^{-1} for each of these microstructures, using the same parameters. The five simulated stress–strain curves for a given number of grains, as well as the evolutions of the contribution of GB sliding to the global strain are compared in Figures 15(b) and (c).

For the model with 15 grains, the difference between the maximum and the minimum predicted GBS contributions was as high as 25 pct. Model #1 and model #3 showed the highest and the lowest contributions of GBS, respectively, which correlated well with their respective highest and lowest cumulated lengths of GBs projected on the maximum shear stress directions, and with the presence of well oriented GBs cutting free surfaces in model #1. Note that the highest contribution of GBS also corresponded to the softest macro-scale response, and *vice versa*. Macro-scale convergence was achieved for 22 grains, and the bias due to the free side surfaces was reduced as well. However, some scatter (approximately 5 pct difference) was still observed in the contribution of GB sliding to the global strain. Microstructures with 30 grains had to be used to get reproducible stress–strain curves as well as reproducible predictions of GBS contribution.

3. *Assumptions made and identification procedure*

As a whole, 12 parameters, some of which temperature-dependent, had to be identified. Out of those, only 10 are actually independent, since K_0 and K_t were deduced from the global elastic moduli. The Young's modulus was identified from the tensile tests at each temperature. The hardening parameters R_0, Q, and b were identified from the room temperature tensile tests. While b was assumed independent of the temperature, R_0 and Q were deduced from the yield stress, at each temperature. The three viscosity parameters of the grains, a, n and the threshold stress σ_c were identified from available tension and relaxation data. An initial guess for the GB sliding proportionality constant, b_t, was obtained by extrapolating the equation provided by Agarwal *et al.*[9] for Al5083 for higher temperatures to the medium temperature range of interest.

C. *Identified Model and Insight into Micro-scale Phenomena*

A comparison of experimental and simulated stress–strain or strain rate-stress curves at each temperature is shown on Figure 16, and the corresponding best-fit sets of parameters are gathered in Table IV.

The model captures the large change in tensile strength with strain rate for the F/UFG material. The simulated relaxation curve at 200 °C nicely reproduces the experimental one, while a less satisfactory agreement is obtained at 100 °C and 150 °C.

The contribution of grain boundary sliding during the simulated tensile tests is plotted *vs* the inelastic strain in Figure 17.

Because the threshold stress for GB sliding ($\approx 2 \times \tau_c$) was always lower than the threshold stresses for plastic and viscous flow inside the grains (R_0 and σ_c, respectively), 100 pct of the inelastic strain was initially accommodated by GB sliding. This fraction then decreased as inelastic deformation developed inside the grains, and tended towards a steady-state value, which was always much larger in the UFG material. Such evolutions bear some similitude with that of the ratio of plastic dissipation due to GBS to the total plastic dissipation computed for nano-crystalline copper by Warner *et al.*[24] using atomistically-informed CPFE. This ratio also started at 100 pct and decreased towards a grain size-sensitive value. As expected, the contribution of GBS was predicted to increase with decreasing strain rate at a given temperature (Figure 17(a)) and with increasing temperature, at a fixed rate (Figure 17(b)).

The SRS computed for the F/UFG material is plotted on Figure 18 *vs* the predicted contribution of GBS to the global inelastic strain, after 10 pct tensile strain, at various rates and temperatures. The experimental data are also plotted for comparison. The model captures the experimentally observed direct correlation.

Journal : MMTA Dispatch : 3-12-2019 Pages : 14
PIPS No. : 5583 LE TYPESET
MS Code : CP DISK

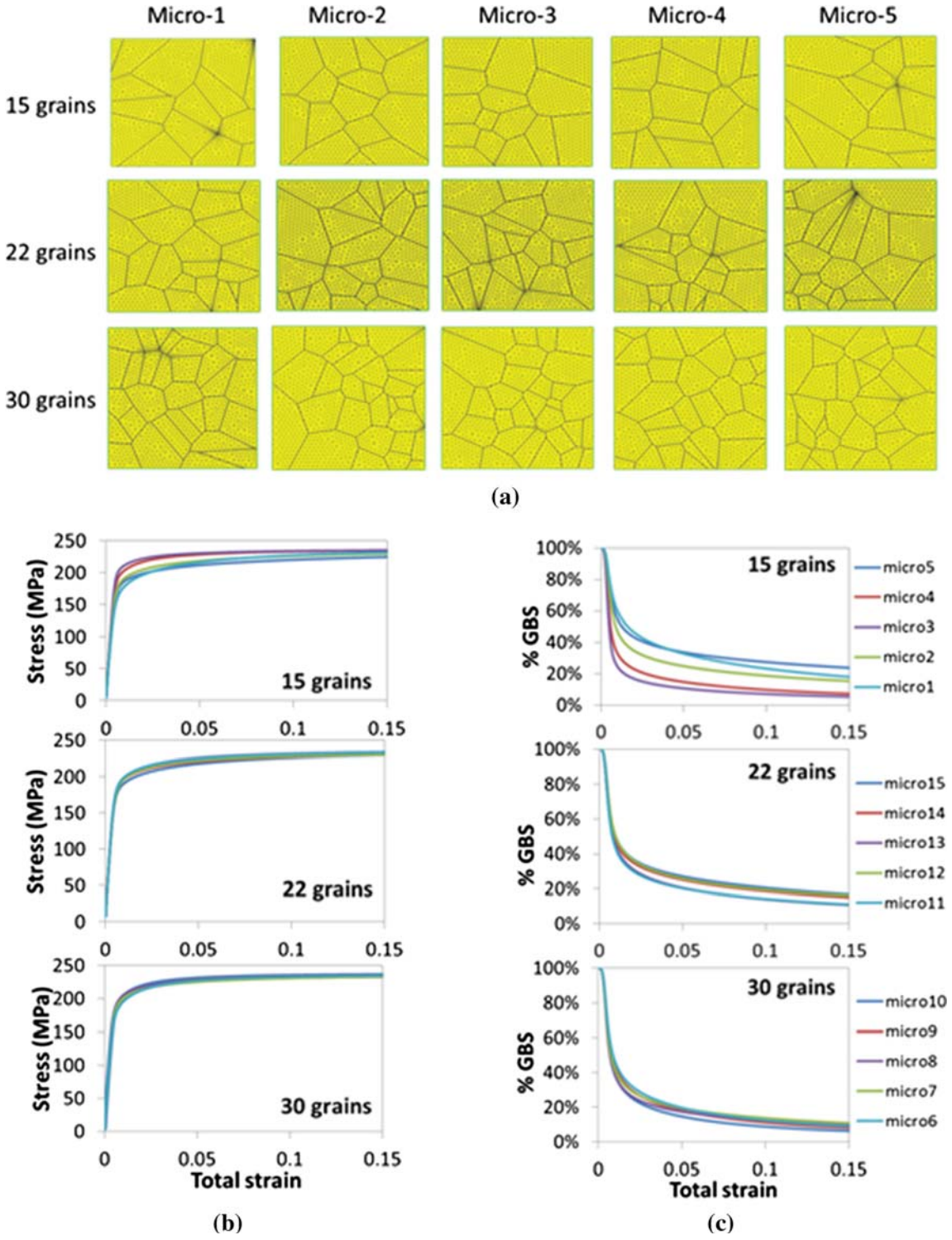

Fig. 15—Convergence study in terms of number of grains: (*a*) meshes, (*b*) computed stress–strain curves, and (*c*) contribution of GBS to the global inelastic strain.

Figure 19 shows the viscous sliding along GBs at various stages of a tensile test at 200 °C and 2×10^{-4} s^{-1}. Initially, GB sliding was triggered by the far field, and thus occurred along GBs oriented close to the maximum shear stress direction (± 45 deg), and often along less constrained, surface-cutting GBs. Upon further straining, sliding was triggered along connected GBs, not as well aligned with the far-field shear stress, and were pushed by an already gliding GB. This led to cooperative GBS along "percolation paths" that sometimes crossed the gage width. This phenomenon

Journal : MMTA Dispatch : 3-12-2019 Pages : 14
PIPS No. : 5583 ☐ LE ☐ TYPESET
MS Code : ☐ CP ☐ DISK

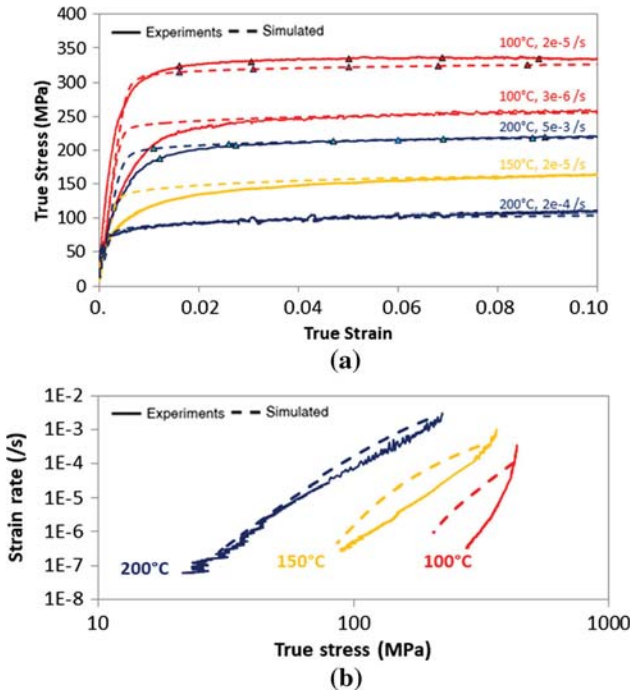

Fig. 16—Experimental and simulated curves for (*a*) tensile and (*b*) relaxation tests on F/UFG material at 100 °C, 150 °C, and 200 °C.

Table IV. Identified Set of Parameters

	100 °C	150 °C	200 °C
E (MPa)	62000	56900	51700
ν	0.3	0.3	0.3
R_0 (MPa)	325	292	225
Q (MPa)	125	75	50
b	45	45	45
a (s^{-1} MPa^{-n})	1.5×10^{-18}	8.5×10^{-14}	2.5×10^{-12}
n	5.5	4	4
σ_c (MPa)	89	48	15
K_n (MPa mm^{-1})	4.26×10^9	3.91×10^9	3.55×10^9
K_t (MPa mm^{-1})	1.64×10^9	1.50×10^9	1.37×10^9
b_t (mm s^{-1} MPa	2×10^{-10}	4.5×10^{-9}	5.0×10^{-8}
τ_c (MPa)	42	10	2

might explain the intense shear bands crossing the whole gage length observed in F/UFG material at high temperature.

Figure 20 reports some simulation results for a tensile test until 10 pct strain at 5×10^{-3} s^{-1} and 200 °C on the more realistic, heterogeneous microstructure shown on Figure 14(c). Figure 20(a) shows the axial viscoplastic strain field, Figure 20(b) shows the viscous sliding along GBs, Figure 20(c) corresponds to the rotation field (antisymmetric part of the displacement gradient), and Figure 20(d) the average rotation in each grain. From Figure 20(a), it appears that in some places (see the enlarged areas), transgranular shear bands are induced by sliding along a neighboring GB, which relaxes the shear stress along the GB, so that this stress is redistributed in the next grain, and triggers viscoplastic

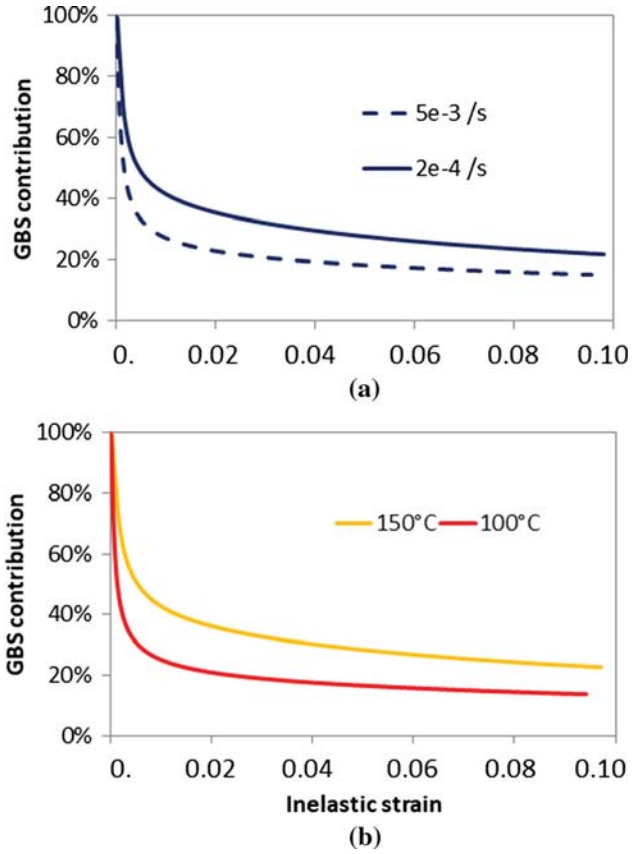

Fig. 17—Predicted effects of (*a*) strain and strain rate at 200 °C and (*b*) strain and temperature at 2×10^{-5} s^{-1} on the contribution of GBS to the global inelastic strain in F/UFG material.

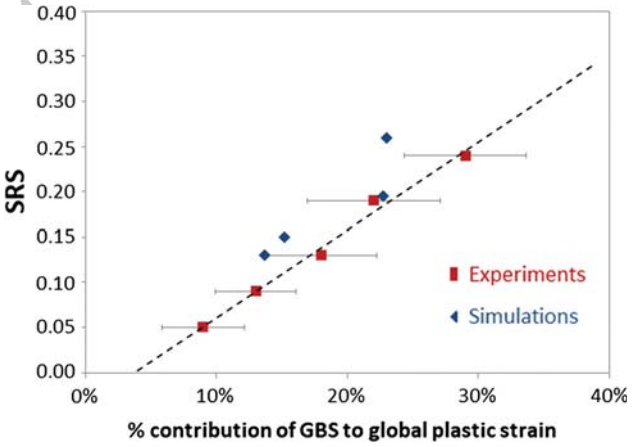

Fig. 18—Correlation between measured/computed SRS and measured/computed contribution of GBS to the global deformation.

flow. This intensified transgranular plastic flow might in turn activate GBS along an GB located on the other side of the grain. Percolation *through the grains* and not only *along the GBs* might thus contribute to the development of long shear bands.

It can also be concluded that GBS increases the heterogeneity of the plastic strain field: a variation from 0.57 to 2.5 times the mean plastic strain is observed here, in spite of similar constitutive equations in all the

Journal : MMTA Dispatch : 3-12-2019 Pages : 14
PIPS No. : 5583 ☐ LE ☐ TYPESET
MS Code : ☐ CP ☐ DISK

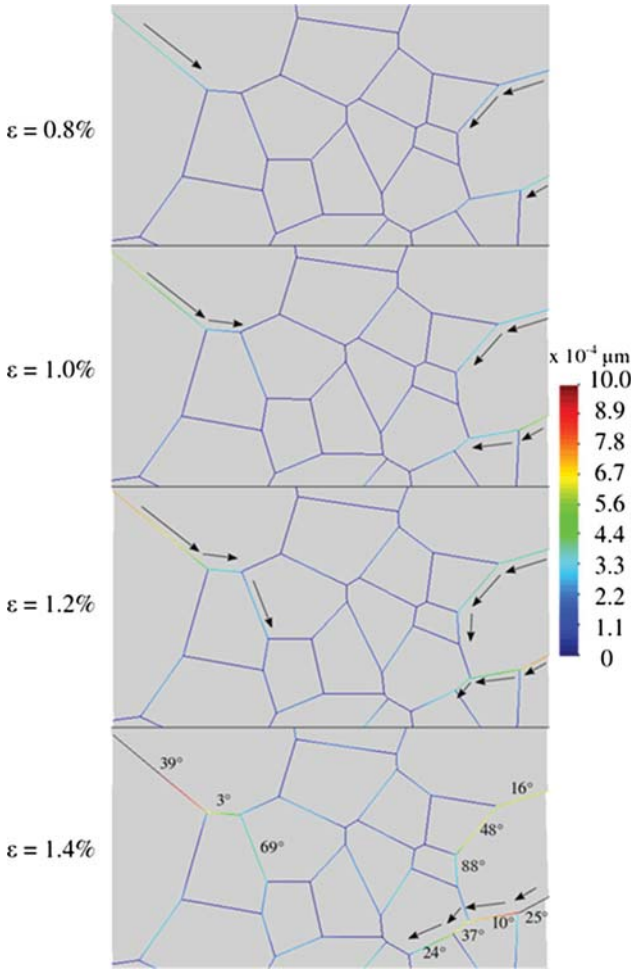

Fig. 19—Viscous sliding along GBs at various steps for a simulation run at 2×10^{-4} s^{-1} and 200 °C in the F/UFG material.

"grains". Such a range is not so far from the range obtained by the statistical analysis of plastic strain fields measured by DIC in the F/UFG material, which was typically 0 to 3 times the mean value.[21]

Time-dependent grains rotation has been shown, through *in situ* SEM or TEM straining and crystal orientation mappings, to contribute significantly to the viscoplastic deformation of UFG materials, even at room temperature[30–32] and to be a collective process, occurring in small groups of neighboring grains.[32] This feature is retrieved by the simulations, as illustrated by Figure 20(d), which shows clusters of grains rotated by up to ± 1.5 deg. Neighboring grains often exhibit rotations of opposite sign (as if they were contacting gears) so that the overall rotation vanishes. The formation of such grain clusters, often inclined by ± 45 deg relative to the tensile axis, might also contribute to the development of shear bands. Figure 20(c) shows that grains do not rotate as a block. The rotation is generally more pronounced near their sliding GBs—where it can reach ± 5 deg, which should lead to an accumulation of geometrically-necessary dislocations—than in their core. Furthermore, GBS and grain rotation are clearly correlated phenomena: grains that do not exhibit GBS do not rotate significantly, and the largest rotations are associated with substantial GBS.

IV. CONCLUSIONS AND PERSPECTIVES

The boundary between the temperature-strain rate domains where the F/UFG Al 5083 alloy is stronger or softer than its CG counterpart was determined and is consistent with data from the literature (Figure 6).

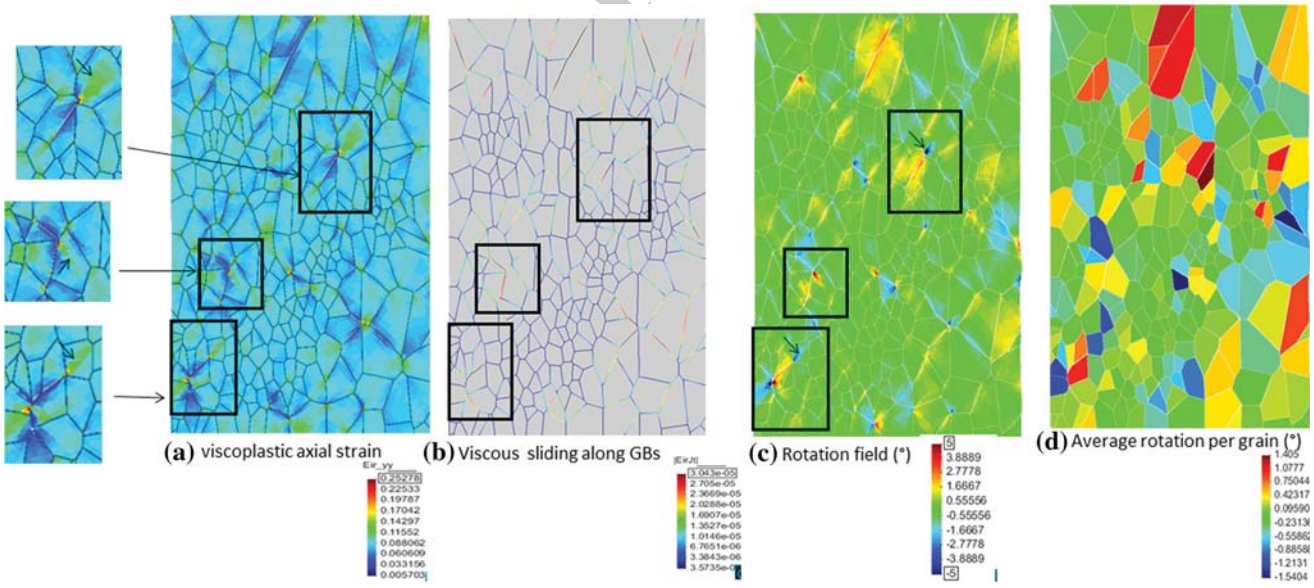

Fig. 20—Results from the simulation of a tensile test at 5×10^{-3} s^{-1} at 200 °C until 10 pct strain on the microstructure from Fig. 14(c).

Journal : MMTA Dispatch : 3-12-2019 Pages : 14
PIPS No. : 5583 ☐ LE ☐ TYPESET
MS Code : ☐ CP ☐ DISK

The SRS of the F/UFG material, which is higher than that of CG material, rises with the temperature and as the strain rate decreases (Figure 5). It is controlled by grain boundary sliding (Figure 13), and controls the ductility, which is thus strongly rate-dependent (Figure 7).

Both CG and F/UFG materials exhibit more and more GBS as the temperature rises and as the strain rate decreases. However, in the former, this mechanism accounts at most for 4 pct of the global strain below 200 °C, while in the latter, its contribution can reach 29 pct (Tables II and III).

A 2D phenomenological FE-model with viscoplastic grains and viscous sliding GBs was developed and identified. It captured the macroscopic behavior of the F/UFG material over a wide range of rates and temperatures.

The model also showed that GBS increases the heterogeneity of the plastic strain field. It provided some insight into the correlated and cooperative mechanisms of GBS and grain rotation that are probably responsible for macro shear banding in the F/UFG material. The simulations suggested that such cooperative phenomena occur along percolation paths that can be intergranular as well as transgranular.

Several further developments of the model can be envisaged: (1) the uniform threshold stress for GB sliding used here might rather be a random variable to capture the differences in GBs ability to slide and (2) a grain size dependence of the model parameters might be introduced. The latter objective would however require a substantial experimental database on several batches of material with different mean grain size, for calibration.

ACKNOWLEDGMENTS

An ECAP facility of LEM3 laboratory in Metz was used to produce the UFG material, under the supervision of Dr. J.J. Fundenberger, who is gratefully acknowledged.

REFERENCES

1. Y. Huang and T.G. Langdon: *Mater. Today*, 2013, vol. 16, pp. 85–93.
2. I. Sabirov, M.R. Barnett, Y. Estrin, and P.D. Hodgson: *Scripta Mater.*, 2009, vol. 61, pp. 181–84.
3. K.V. Ivanov and E.V. Naydenkin: *IOP Conf. Ser. Mater. Sci. Eng.*, 2014, vol. 63, pp. 1–10.
4. R.C. Gifkins, A. Gittins, R.L. Bell, and T.G. Langdon: *J. Mater. Sci.*, 1968, vol. 3, pp. 306–13.
5. A. Arieli and A.K. Mukherjee: *Mater. Sci. Eng.*, 1980, vol. 45, pp. 61–70.
6. Y.G. Ko, D.H. Shin, K.T. Park, and C.S. Lee: *Mater. Sci. Eng. A*, 2007, vols. 448–451, pp. 756–60.
7. K.-T. Park, D.Y. Hwang, S.-Y. Chang, and D.H. Shin: *Metall. Mater. Trans. A*, 2002, vol. 33A, pp. 2859–67.
8. K.T. Park, H.J. Lee, C.S. Lee, B.D. Ahn, H.S. Cho, and D.H. Shin: *Mater. Trans.*, 2004, vol. 45, pp. 958–63.
9. S.Y. Chang, L. Jung Guk, K.T. Park, S. Dong Hyuk, J.G. Lee, K.T. Park, and D.H. Shin: *Mater. Trans.*, 2001, vol. 42, pp. 1074–80.
10. R. Kapoor and J.K. Chakravartty: *Acta Mater.*, 2007, vol. 55, pp. 5408–18.
11. R. Raj and M.F. Ashby: *Metall. Trans.*, 1971, vol. 2, pp. 1113–27.
12. M.F. Ashby and R.A. Verrall: *Acta Metall.*, 1973, vol. 21, pp. 149–63.
13. F. Crossman and M.F. Ashby: *Acta Metall.*, 1975, vol. 23, pp. 425–40.
14. V. Tvergaard: *J. Mech. Phys. Solids*, 1985, vol. 33, pp. 447–69.
15. V. Tvergaard: *Rev. Phys. Appl.*, 1988, vol. 23, pp. 595–604.
16. K.J. Hsia, D.M. Parks, and A.S. Argon: *Mech. Mater.*, 1991, vol. 11, pp. 43–62.
17. P. Onck and E. Van der Giessen: *Int. J. Solids Struct.*, 1997, vol. 34, pp. 703–26.
18. A.F. Bower and E. Wininger: *J. Mech. Phys. Solids*, 2004, vol. 52, pp. 1289–1317.
19. S. Agarwal, C.L. Briant, P.E. Krajewski, A.F. Bower, and E.M. Taleff: *J. Mater. Eng. Perform.*, 2007, vol. 16, pp. 170–78.
20. N. Du, A.F. Bower, P.E. Krajewski, and E.M. Taleff: *Mater. Sci. Eng. A*, 2008, vol. 494, pp. 86–91.
21. A. Goyal, Mechanical behaviour of ultra-fine grain Al 5083 alloy: Analysis and modelling of the role of grain boundaries to overall plastic deformation., Ph.D. Thesis, Ecole Polytechnique, Palaiseau, France, 2018.
22. Y. Qi and P.E. Krajewski: *Acta Mater.*, 2007, vol. 55, pp. 1555–63.
23. N. Du, Y. Qi, P.E. Krajewski, and A.F. Bower: *Metall. Mater. Trans. A*, 2011, vol. 42A, pp. 651–59.
24. D.H. Warner, F. Sansoz, and J.F. Molinari: *Int. J. Plast.*, 2006, vol. 22, pp. 754–74.
25. L. Allais, M. Bornert, T. Bretheau, and D. Caldemaison: *Acta Metall. Mater.*, 1994, vol. 42, pp. 3865–80.
26. D. Lee: *Metall. Trans.*, 1971, vol. 2, pp. 1245–48.
27. R. Kapoor, C. Gupta, G. Sharma, and J.K. Chakravartty: *Scripta Mater.*, 2005, vol. 53, pp. 1389–93.
28. R.L. Bell, C. Graeme-Barber, and T.G. Langdon: *Trans. Metall. Soc. AIME*, 1967, vol. 239, pp. 1821–23.
29. Fracsima, Disroc, a Finite Element Code for modelling Thermo-Hydro-Mechanical processes in fractures porous media. 2016. http://www.fracsima.com/DISROC/Disroc.html.
30. Yu. Ivanisenko, N.A. Enikeev, K. Yang, A. Smoliakov, V.P. Soloviev, and H. Fecht: *Mater. Sci. Eng. A*, 2016, vol. 668, pp. 255–62.
31. E. Izadi, A. Darbal, R. Sarkar, and J. Rajagopalan: *Mater. Des.*, 2017, vol. 113, pp. 186–94.
32. F Mompiou and M Legros: *Scripta Mater.*, 2015, vol. 99, pp. 5–8.

Journal : MMTA Dispatch : 3-12-2019 Pages : 14
PIPS No. : 5583 ☐ LE ☐ TYPESET
MS Code : ☐ CP ☐ DISK